



# CHORUS

This is the accepted manuscript made available via CHORUS. The article has been published as:

## Tunable Superconducting Qubits with Flux-Independent Coherence

M. D. Hutchings, J. B. Hertzberg, Y. Liu, N. T. Bronn, G. A. Keefe, Markus Brink, Jerry M. Chow, and B. L. T. Plourde

Phys. Rev. Applied **8**, 044003 — Published 12 October 2017

DOI: [10.1103/PhysRevApplied.8.044003](https://doi.org/10.1103/PhysRevApplied.8.044003)

# Tunable Superconducting Qubits with Flux-Independent Coherence

M. D. Hutchings,<sup>1</sup> J. B. Hertzberg,<sup>2</sup> Y. Liu,<sup>1</sup> N. T. Bronn,<sup>2</sup> G. A. Keefe,<sup>2</sup> Markus Brink,<sup>2</sup> Jerry M. Chow,<sup>2</sup> and B. L. T. Plourde<sup>1</sup>

<sup>1</sup>*Syracuse University, Department of Physics, Syracuse, NY 13244, USA*

<sup>2</sup>*IBM, T J Watson Research Center, Yorktown Heights, NY 10598, USA*

(Dated: August 20, 2017)

We have studied the impact of low-frequency magnetic flux noise upon superconducting transmon qubits with various levels of tunability. We find that qubits with weaker tunability exhibit dephasing that is less sensitive to flux noise. This insight was used to fabricate qubits where dephasing due to flux noise was suppressed below other dephasing sources, leading to flux-independent dephasing times  $T_2^* \sim 15 \mu\text{s}$  over a tunable range of  $\sim 340$  MHz. Such tunable qubits have the potential to create high-fidelity, fault-tolerant qubit gates and fundamentally improve scalability for a quantum processor.

## I. INTRODUCTION

Quantum computers have the potential to outperform classical logic in important technological problems. A practical quantum processor must be comprised of quantum bits (“qubits”) that are isolated from environmental decoherence sources yet easily addressable during logical gate operations. Superconducting qubits are an attractive candidate because of their simple integration with fast control and readout circuitry. In recent years, advances in superconducting qubits have demonstrated how such integration may be achieved while maintaining high coherence [1–3]. Further extensions of qubit coherence will serve to reduce gate errors, cutting down the number of qubits required for fault-tolerant quantum logic [4, 5].

An important aspect of maintaining high qubit coherence is the reduction of dephasing. Frequency-tunable qubits are inherently sensitive to dephasing via noise in the tuning control channel. Tuning via a magnetic flux thus introduces dephasing via low-frequency flux noise [6–13]. Such noise is ubiquitous in thin-film superconducting devices at low temperatures. Experiments indicate a high density of unpaired spins on the thin-film surface [14] with fluctuations of these leading to low-frequency flux noise that typically has a  $1/f$  power spectrum [13, 15–17]. For any flux-tunable qubit, this flux noise leads to significant dephasing whenever the qubit is biased at a point with a large gradient of the qubit energy with respect to flux.

Flux tuning is nonetheless highly advantageous for many quantum circuits, and several classes of quantum logic gates rely on flux-tunable qubits. In the controlled-phase gate [1, 18], qubit pairs are rapidly tuned into resonance to create entanglement. Here, both flux noise and off-resonant coupling to other qubits produce phase errors proportional to gate times, with total gate error scaling as the square of the gate time [19]. Alternatively, fixed-frequency qubits have been employed in schemes such as the cross resonance (CR) gate [20, 21] to demonstrate aspects of quantum error correction (QEC) [3, 22]. Recent efforts with two-qubit devices have extended CR

gate fidelities beyond 99% [23]. Larger lattices of fixed-frequency qubits, however, are likely to suffer increasingly from frequency crowding. If a qubit’s 0-1 excitation frequency overlaps with the 0-1 or 1-2 frequency of its neighbor, or if the two qubits’ frequencies are very far apart, the CR gate between these two qubits will be non-ideal, with the strong possibility of leakage out of the computational subspace, or a very weak gate, respectively [24]. However, fixed-frequency transmon qubits are challenging to fabricate to precision better than about 200 MHz [25]. Given such imprecision, a hypothetical seventeen-qubit logic circuit could see up to a quarter of its gate pairs fail due to frequency crowding (see Appendix A). Frequency-tunable transmon qubits therefore appear attractive for use in architectures based on the CR gate.

In this paper, we show how a tunable qubit’s sensitivity to flux noise may be reduced by limiting its extent of tunability. We report results for several different qubits showing that the qubit dephasing rate is proportional to the sensitivity of the qubit frequency to magnetic flux and to the amplitude of low-frequency flux noise. Furthermore, we use the understanding gained through this study to fabricate a qubit whose dephasing due to non-flux dependent sources exceeds its dephasing due to low-frequency flux noise, over a range of more than 300 MHz of tunability. This unique qubit has the potential to reduce errors in gates employing frequency-tunable qubits and to evade frequency crowding in qubit lattices employing CR gates. It therefore offers a promising route to create high-fidelity two-qubit gates that reach fault-tolerant gate operation and to improve the scalability of superconducting qubit devices.

Our device adapts a design in which a superconducting quantum interference device (SQUID) serves as the Josephson inductance in a transmon qubit [26]. Here, the Josephson energy, and consequently the qubit 0-1 transition frequency  $f_{01}$ , may be tuned with a magnetic flux  $\Phi$  with a period of  $\Phi_0 \equiv h/2e$ , the magnetic flux quantum, where  $h$  is Planck’s constant and  $e$  is the electron charge. However, if the two junctions in the SQUID have different Josephson energies  $E_{J1}$  and  $E_{J2}$ , a so-called ‘asymmetric

transmon' is formed [27]. The greater the difference in junction energies, the smaller the level of tunability. If  $E_{J1} > E_{J2}$ , we can define the ratio  $\alpha = E_{J1}/E_{J2}$  and the sum  $E_{J\Sigma} = E_{J1} + E_{J2}$ . The total flux-dependent Josephson energy  $E_J$  varies according to the following expression from Ref. [26]:

$$E_J(\Phi) = E_{J\Sigma} \cos\left(\frac{\pi\Phi}{\Phi_0}\right) \sqrt{1 + d^2 \tan^2\left(\frac{\pi\Phi}{\Phi_0}\right)}, \quad (1)$$

where  $d$  is given by  $d = (\alpha - 1)/(1 + \alpha)$ .

## II. DEVICE DESIGN AND FABRICATION

Considering that qubits on a single chip should experience a common flux noise level, we prepared two styles of sample, A and B, shown in Fig. 1. We varied  $\alpha$  on sample A to observe the effect on dephasing and included fixed-frequency qubits on both samples as a reference for non-flux dependent dephasing. Each chip included eight separate cavity/qubit systems in a multi-qubit planar circuit quantum electrodynamics (cQED) architecture. Sample A included transmon qubits of the design found in Refs. [3, 22], with readout resonators frequency-multiplexed and coupled to a common feedline for microwave drive and readout. Sample B employed the qubit design of Refs. [23, 28, 29], with a separate microwave port for each readout resonator. On sample B, coplanar-waveguide buses, resonant at  $\sim 6$  GHz, couple the qubits together three at a time to form a lattice for multi-qubit gate operations, as in Refs. [28] and [29], although no such operations are presented in this paper. On sample A we adjusted junction areas to prepare transmons having junction ratios  $\alpha = 7, 4,$  and  $1$ . To keep  $E_{J\Sigma}$  fixed among the qubits, we kept total junction area fixed, while the single-junction qubit maintained the same SQUID loop structure with one of the junctions being left open. On sample B, we designed six qubits to have  $\alpha = 15$  while two employed a single junction matching the  $E_{J1}$  of the tunable qubits.

To fabricate both sample A and B we used standard photolithography and plasma-etching to pattern the coplanar waveguides, ground plane, and qubit capacitors from a sputtered Nb film on a Si substrate. On sample A the Nb films are 100 nm thick. On sample B they are 200 nm. Electron-beam lithography and conventional double-angle shadow-evaporation was used to form Al-AlO<sub>x</sub>-Al tunnel junctions and the traces connecting them to the transmon shunt capacitors. In samples A and B, the differing separation between capacitor pads necessitated different SQUID loop geometries, as shown in Fig. 1. Effects of loop geometry on flux noise have been the subject of recent studies [30, 31]. On sample A, the SQUID loops comprised  $0.6 \mu\text{m}$  wide Al traces bridging the  $20 \mu\text{m}$  gap between transmon capacitor pads, and we adjusted the junction area by adjusting the junction

width, keeping the overlap fixed at  $0.2 \mu\text{m}$ . On sample B, SQUID loops had  $2 \mu\text{m}$  trace width and joined to Nb leads extending from the capacitor pads, which had a  $70 \mu\text{m}$  separation. On sample B, we adjusted the junction sizes via both width and overlap. On both samples A and B, the SQUID loop area is  $\sim 400 \mu\text{m}^2$ .

## III. EXPERIMENT

Measurements of sample A were completed in a dilution refrigerator (DR) at Syracuse University (SU), while sample B was measured in a DR at the IBM TJ Watson Research Center. Samples were wire-bonded into holders designed to suppress microwave chip modes, mounted to the mixing chamber of the DR and placed inside a cryoperm magnetic shield, thermally anchored at the mixing chamber. Both DRs incorporated room-temperature  $\mu$ -metal shields.

For sample A, room-temperature microwave signals were supplied through attenuated coaxial lines, thermalized at each stage of the DR and filtered using 10 GHz low pass filters (K&L) thermalized at the mixing chamber. We used a total of 70 dB of attenuation on the drive-lines: 20 dB at 4 K, 20 dB at 0.7 K and 30 dB at the mixing chamber, with a base temperature of 30 mK. Output measurement signals from the sample pass through another 10 GHz low-pass filter, a microwave switch, and two magnetically shielded cryogenic isolators, all thermally anchored to the mixing chamber. In the case of sample A, the signal was amplified by a low-noise HEMT at 4 K, passing through a Nb/Nb superconducting coaxial cable between the mixing chamber and 4 K stage. The signal was amplified further at room temperature before being mixed down to 10 MHz and digitized. The eight resonators, coupled to each of their respective qubits on sample A, had measured frequencies that ranged from 6.975 – 7.136 GHz, separated by  $\sim 20 - 25$  MHz. Linewidths  $\kappa/2\pi$  for these resonators were on the order of a few hundreds of kHz.

Figure 1 shows the layout of the sample B chip. The  $\alpha = 15$  asymmetric-SQUID transmon reported in this paper was located at position  $Q_7$ . It was read out through a coplanar waveguide resonator of frequency 6.559 GHz and linewidth  $\sim 300$  kHz, and was found to have  $f_{01}^{max} = 5.387$  GHz. The fixed-frequency transmon (5.346 GHz) at position  $Q_2$  was read out through a 6.418 GHz resonator having linewidth  $\sim 300$  kHz. Sample B qubits were measured via signal wiring similar to that presented in Refs. [3, 22, 28, 32]. Drive wiring included 10 dB of attenuation at 50 K, 10 dB at 4K, 6 dB at 0.7 K, 10 dB at 100 mK, and at the mixing-chamber plate there was 30 dB of attenuation plus a homemade 'Eccosorb' low-pass filter. Drive signals entered a microwave circulator at the mixing plate. On one set of signal wiring, the 2nd port of the circulator passed directly to qubit  $Q_7$ . In another set of signal wiring, the second port of the circulator passed to several different qubits via a mi-

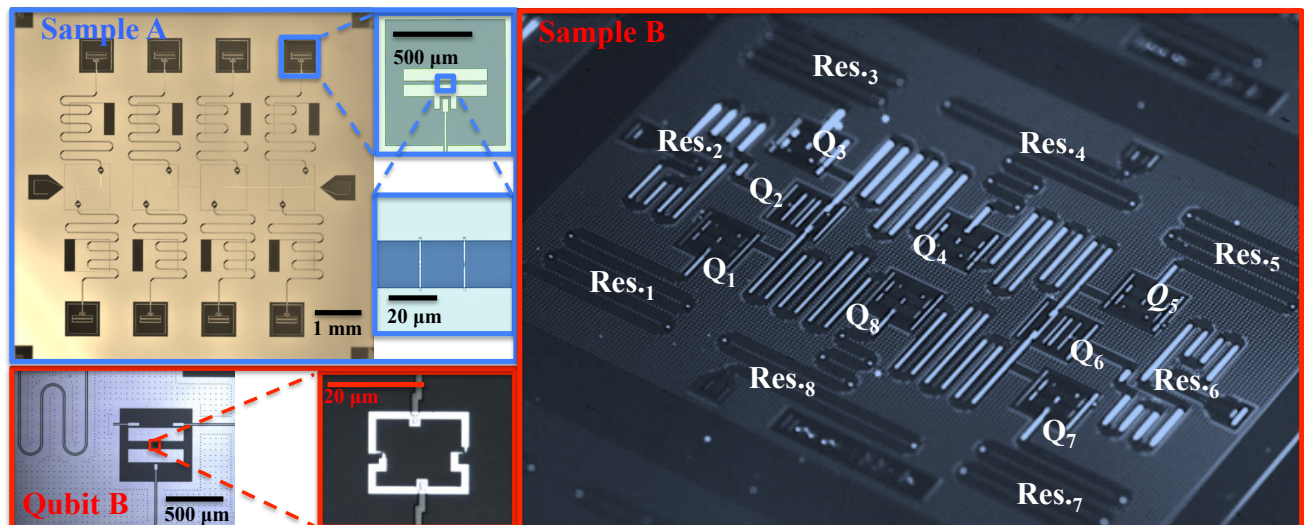


FIG. 1. Optical micrographs of samples including higher magnification images of qubits and SQUID loops. Sample B image is a chip of identical design to the ones used for measurements. In sample B image, labels indicate each qubit and its individual readout resonators, while unlabeled resonators are bus resonators.

crowdave switch. Signals reflected from the device passed back through the circulator to the output and amplifier circuitry. Output circuitry comprised a low-pass Cu powder filter, followed by two cryogenic isolators in series, followed by an additional low-pass filter, followed by superconducting NbTi coaxial cable, followed by a low-noise HEMT amplifier at 4 K and an additional low-noise amplifier at room temperature. Low-pass filters were intended to block signals above  $\sim 10$  GHz. In the case of  $Q_7$ , additional amplification was afforded by a SLUG amplifier [33] mounted at the mixing stage, biased via two bias-tee networks and isolated from the sample by an additional cryogenic isolator. Output signals were mixed down to 5 MHz before being digitized and averaged. The mixing-plate thermometer indicated a temperature of  $\sim 15$  to 20 mK during measurements.

Magnetic flux was supplied to sample A via a  $\sim 6$ -mm inner diameter superconducting wire coil placed 2 mm above the sample and fed via brass coaxial lines thermally anchored at each stage of the DR, with a 80 MHz  $\pi$ -filter at 4 K and a copper powder filter on the mixing chamber. Sample B was flux-biased using a wire-wound superconducting coil mounted about 3 mm above the qubit chip and fed via DC pair wiring (Cu above 4K within the fridge, NbTi below). The coil had a self-inductance of 3.9 mH and mutual inductance to the SQUID loop of  $\sim 1$  pH. Coils were current-biased using SRS SIM928 DC voltage sources through a 2 k $\Omega$  or 5 k $\Omega$  room-temperature resistor. DC flux was applied simultaneously to all qubits on a chip. For each qubit, we measured  $f_{01}$  as a function of coil current and fit this against Eq. (1) to enable scaling of  $\Phi_0$  and subtract any offset flux, as well as to determine  $f_{01}^{max}$  and asymmetry  $d$ . We treat the sign of flux as arbitrary. We observed no evidence of ohmic heating due to current-biasing the coils. In particular, over

the range of applied fluxes we observed negligible change in fridge temperature, no trend in the coherence of fixed-frequency qubits, and no trend in the tunable qubits that was consistent with heating. Our use of superconducting coils and cabling, and thermal anchoring of cabling, was effective in this regard.

Coherence measurements for both samples were performed using standard cQED readout techniques [34]. The flux level was set prior to qubit measurement and held fixed during the measurement. Using an automated measurement algorithm, qubit frequency was determined using Ramsey fringe fitting, after which  $\pi$  and  $\pi/2$  pulses were optimized at this frequency, and then coherence was measured.  $T_2^*$  was measured at a frequency-detuning that offered sufficient fringes for fitting. If the automated tuning routine failed to find the frequency or properly scale the  $\pi$  and  $\pi/2$  pulses, this point was omitted from the dataset. All coherence data was visually checked before fitting and inclusion in the dataset.

#### IV. RESULTS AND DISCUSSION

From the eight qubits on each chip, we present data from four qubits on sample A and two qubits on sample B, one of each variation from each sample. Figure 2 shows the flux dependence of  $f_{01}$ , subtracting fixed flux offsets for each qubit. The  $\alpha = 15$  qubit had the weakest tunability: 337 MHz. Following Eq. (1) and the expectation that  $f_{01} \propto \sqrt{E_J}$  [26], we fit the data in Fig. 2 to find the maximum frequency  $f_{01}^{max} \propto \sqrt{E_{J\Sigma}}$  and asymmetry parameter  $d$ . From the latter we compute  $\alpha$  and find that all qubits' measured asymmetry values were within 5% of the designed values. We note that the four sample

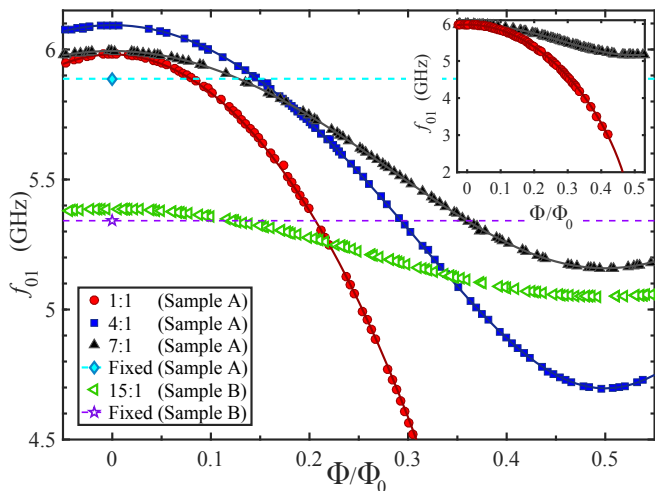


FIG. 2.  $f_{01}$  vs. flux measured for qubits from samples A and B. Solid lines are fits to these tuning curves based on Eq. (1). Also included are frequencies of single junction qubits from both samples. Dashed lines for these qubits to guide the eye. Inset: entire tuning range measured for the  $\alpha = 1$  qubit with the  $\alpha = 7$  qubit included as a comparison to illustrate the large frequency tunability of an  $\alpha = 1$  qubit.

A qubits shown in Fig. 2 were designed to have identical  $E_{J\Sigma}$  and therefore identical  $f_{01}^{\max}$ , but in fact exhibit a  $\sim 200$  MHz spread, thus illustrating the challenge of fabricating qubits to precise frequencies.

To assess the effect of flux noise on dephasing, we observe how the latter relates to each qubit’s frequency gradient as a function of flux  $D_\Phi = |\partial f_{01}/\partial \Phi|$ . We characterize dephasing via measurement of the Ramsey decay time  $T_2^*$ , which is sensitive to low-frequency dephasing noise [7, 9]. We fit these using an exponential form. Although it has been shown that a dephasing noise source with a  $1/f$  power spectrum will result in a Gaussian decay envelope [7, 9], flux-independent dephasing sources such as cavity-photon shot-noise [35–37] result in an exponential decay envelope. Ramsey decays for fixed-frequency qubits are therefore well fit with an exponential decay envelope. For all of our asymmetric transmons, as well as a large portion of the dephasing data for the  $\alpha = 1$  symmetric device, we find that an exponential decay envelope is also a good fit. As detailed in Appendix D, we find systematic but slight differences between values of  $T_2^*$  obtained using an exponential or Gaussian fit. Assuming a purely exponential decay sets an upper bound on the extracted flux noise level.

Relaxation times  $T_1$  ranged from  $\sim 20 - 50 \mu\text{s}$  over the six qubits reported here. In general  $T_1$  increased with decreasing qubit frequency (Appendix B, Fig. 5), consistent with dielectric loss and a frequency-independent loss tangent, as observed in other tunable superconducting qubits [38]. Qubits on sample A remained sufficiently detuned below their readout resonators to neglect Purcell relaxation, but the  $T_1$  of the  $\alpha = 15$  qubit on sample B exhibits frequency-dependence consistent with Purcell

losses.  $T_1$  relaxation due to coupling to a flux-bias line, first discussed for inductive coupling in Ref. [26], and for capacitive coupling in Ref. [39], was considered for the qubits studied here. We show in Appendix C that flux-line coupling to our qubits sets an upper bound on  $T_1$  not significantly lower than that reported in Ref. [26], and still orders of magnitude greater than current experimental  $T_1$  times.

To compare dephasing rates among the qubits, we use the relation  $\Gamma_\phi = 1/T_2^* - 1/2T_1$  [40] to remove the relaxation contribution. The resulting dephasing rate  $\Gamma_\phi$  is plotted against flux in Fig. 3. As the curves in Fig. 2 illustrate, the integer and half-integer  $\Phi/\Phi_0$  points are ‘sweet spots’ where  $D_\Phi = 0$  and thus the qubit is first-order insensitive to flux noise. All the transmons on sample A clearly exhibit a dephasing rate that increases with  $D_\Phi$  and is a minimum at the sweet spots. Second-order sensitivity to flux noise [9, 41] should be negligible in our samples because of the small energy-band curvature. However, the level of  $\Gamma_\phi$  for the non-tunable qubit on each sample and the tunable qubits at their sweet spots indicates the presence of non-flux dependent sources of dephasing. Such background dephasing may arise from other mechanisms, including cavity-photon shot noise [35], critical current noise [42], or charge noise affecting the residual charge dispersion in the transmon design [26]. This background dephasing may be expected to vary from qubit to qubit due to differences in qubit-cavity coupling or cavity thermalization, among other effects. Such variations are commonly observed in multi-qubit devices [3, 22, 28].

We note that the behavior of the other qubits on our chips, where it could be measured, is consistent with the six devices presented here. On sample A, the position of the flux coil on the sample holder enabled only one each of the  $\alpha = 4$  and  $\alpha = 7$  transmons to be tuned through a full flux quantum; these appear in the figures. The  $\alpha = 1$  qubit not shown in the figures had an anomalously high background dephasing rate, making its flux-noise dephasing difficult to distinguish. The single-junction transmon not shown in the figures had dephasing  $\Gamma_\phi = 0.102 \mu\text{s}^{-1}$ . On sample B we measured dephasing of three  $\alpha = 15$  qubits and two single-junction qubits. None of the tunable qubits exhibited any flux-dependence in its dephasing. The qubit of each type having the lowest dephasing rate is shown in the figures. The single-junction qubit not shown in the figures exhibited dephasing of  $0.129 \mu\text{s}^{-1}$ , while the mean dephasing rates of the tunable qubits not shown in the figures were  $0.110$  and  $0.144 \mu\text{s}^{-1}$ .

For sample A, if we consider only flux-dependent dephasing, it is evident that  $\Gamma_\phi \propto D_\Phi$ . Furthermore, qubits of the same geometry on the same chip should experience similar flux noise [14]. The analysis outlined in Ref. [7, 9] may then be used to extract a flux noise level from the relationship between  $\Gamma_\phi$  and  $D_\Phi$ . We apply a simultaneous fit of the form  $mD_\Phi + b$  to the  $\alpha = 1, 4,$  and  $7$  qubits, allowing background dephasing  $b$  to vary for each qubit, while a single  $m$  is common to all. The fit appears as solid

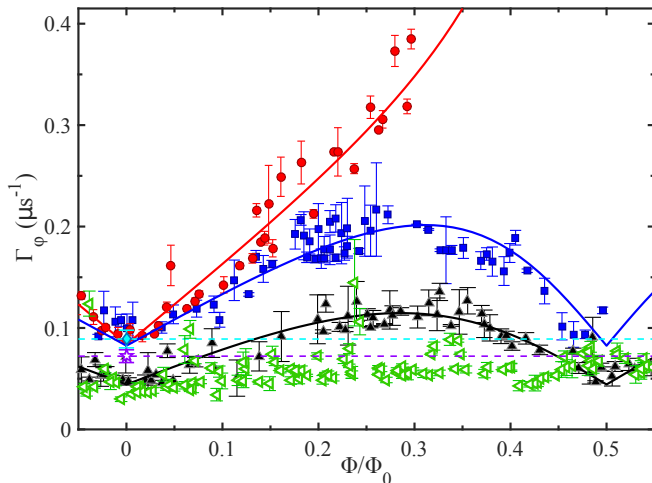


FIG. 3.  $\Gamma_\phi$  vs. flux measured for qubits from samples A and B. Solid lines show a simultaneous fit of the form  $mD_\Phi + b$  to the tunable qubits on sample A. Factor  $m$  is common to all three datasets while  $b$  is allowed to vary for each.  $\Gamma_\phi$  measured for fixed frequency qubits on both samples included with dashed lines to help guide the eye.

lines in Fig. 3. We derive  $\Gamma_\phi = 2\pi\sqrt{A_\Phi|\ln(2\pi f_{IR}t)|}D_\Phi$  following the approach in Ref. [9], where the flux noise power spectrum is  $S_\Phi(f) = A_\Phi/|f|$ ,  $f_{IR}$  is the infrared cutoff frequency, taken to be 1 Hz and  $t$  is on the order of  $1/\Gamma_\phi$ , which we take to be  $10\mu\text{s}$  in our calculations. Equating  $mD_\Phi$  to  $\Gamma_\phi$  in the equation above, we may calculate the flux noise level on sample A. To determine the uncertainty in the measured flux noise level, we must not only account for the error in fitting  $m$  but also how variations in dephasing time impact the calculation of  $A_\Phi$  values. To account for the latter, we determine the impact on extracted  $A_\Phi^{1/2}$  as  $t$  is varied. Adjusting  $t$  over a range similar to what we observe experimentally leads to a  $\sim 10\%$  change in  $A_\Phi^{1/2}$ . The errors we report for all calculated  $A_\Phi^{1/2}$  reflect this added uncertainty. The choice of  $f_{IR} = 1\text{ Hz}$  is related to the typical measurement time for a Ramsey decay. Variations in the value for this cutoff frequency have only a weak impact on the extracted value of  $A_\Phi^{1/2}$ . We find that  $A_\Phi^{1/2} = 1.4 \pm 0.2 \mu\Phi_0$  on sample A. This level is compatible with previous experimental studies of flux noise in superconducting flux [6–8, 43, 44] and phase qubits [45].

To achieve an even clearer picture of the influence of flux noise on these qubits, we plot  $\Gamma_\phi$  vs.  $D_\Phi$  for each qubit in Fig. 4a. Here,  $D_\Phi$  is computed from the fits to the energy bands of each qubit shown in Fig. 2. This yields a linear dependence where the slope can be related to the amplitude of the flux noise and the offset corresponds to the background dephasing level. In this case, instead of a simultaneous fit we apply a separate fit of  $\Gamma_\phi = mD_\Phi + b$  to each qubit, and we find  $A_\Phi^{1/2}$  values of  $1.3 \pm 0.2$ ,  $1.2 \pm 0.2$  and  $1.4 \pm 0.2 \mu\Phi_0$  for the  $\alpha = 7, 4$  and 1 qubits, respectively. These flux noise levels are all

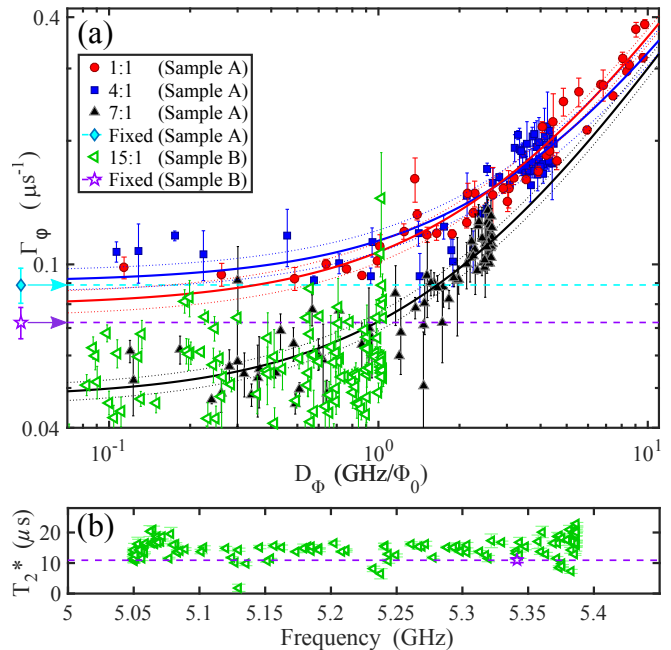


FIG. 4. (a)  $\Gamma_\phi$  vs.  $D_\Phi$  measured for qubits from samples A and B. Solid lines show individual linear fits to the tunable qubits on sample A, as described in text. Note the scale is log-log.  $\Gamma_\phi$  measured for fixed-frequency qubits on both samples, included with dashed lines to help guide the eye. (b)  $T_2^*$  vs. frequency measured for the  $\alpha = 15$  and fixed-frequency qubits on sample B.

consistent with past studies of low-frequency flux noise in superconducting devices [6–8, 43–45].

In Fig. 4a it can be seen that, for the tunable qubits on sample A, within the range  $D_\Phi \lesssim 1\text{ GHz}/\Phi_0$ , the measured dephasing rate is largely flux-independent within the experimental spread. To exploit this insensitivity, we designed the tunable transmon on sample B to have  $D_\Phi$  no greater than  $\sim 1\text{ GHz}/\Phi_0$  at any point within its tuning range, a condition satisfied by having  $\alpha = 15$ . As a result, its sensitivity to  $1/f$  flux noise appears to be suppressed below the level where background dephasing dominates.  $\Gamma_\phi$  is essentially flat across the entire tuning range, as shown in Fig. 3, with a mean of  $0.058\mu\text{s}^{-1}$  and experimental scatter of  $\sigma \sim 0.017\mu\text{s}^{-1}$ . In comparison, this sample’s fixed-frequency qubit exhibits  $\Gamma_\phi = 0.072\mu\text{s}^{-1}$ . Figure 4b shows clearly that  $T_2^*$  for the  $\alpha = 15$  qubit on sample B is independent of frequency over the whole tuning range.

Although no significant flux dependence of the dephasing is detectable for sample B, we estimate from our earlier expression for  $\Gamma_\phi$  that the observed scatter is consistent with  $A_\Phi^{1/2}$  of  $0.9\mu\Phi_0$ . Recent progress in understanding the origins of  $1/f$  flux noise in SQUIDs [46] has facilitated up to a  $5\times$  reduction in  $A_\Phi$ [47]. Such reductions applied to the sample B qubit would reduce its maximum flux-noise-driven dephasing below  $0.008\mu\text{s}^{-1}$ . In a  $\alpha = 7$  qubit tunable over more than 700 MHz, flux

noise of such a level would cause dephasing no greater than  $0.017 \mu\text{s}^{-1}$ . Alternatively, in a qubit with 150 MHz tunability, the flux noise seen in sample B would cause dephasing not exceeding  $0.008 \mu\text{s}^{-1}$ , or only  $0.004 \mu\text{s}^{-1}$  if the flux noise were reduced as in Ref. [47]. We may contrast these values with the non-flux-noise-driven dephasing seen in state-of-the-art single-junction transmons used for multi-qubit gate operations:  $\Gamma_\phi = 0.004$  to  $0.008 \mu\text{s}^{-1}$  on 2-qubit samples [23, 32],  $0.01 \mu\text{s}^{-1}$  on 5-qubit samples [29] and 0.01 to  $0.021 \mu\text{s}^{-1}$  on 7-qubit samples [28]. We also note that the two SQUID designs A and B (Fig. 1), within experimental uncertainties exhibit no difference in flux noise level.

## V. CONCLUSIONS

In conclusion, we have shown that by reducing the flux-tunability of a transmon qubit, we can dramatically lower its sensitivity to  $1/f$  flux noise. Using this understanding, we have fabricated a qubit in which the dephasing rate due to flux noise is suppressed below the level set by non-flux dependent sources. This device exhibits a flux-independent dephasing rate  $\Gamma_\phi \sim 0.06 \mu\text{s}^{-1}$  over a tunable range in excess of 300 MHz.

As qubit architectures progress in complexity, frequency crowding and flux-noise dephasing will present increasing challenges to gate fidelity. A recently demonstrated quantum computing prototype employed nine individually-flux-tuned superconducting qubits [2]. The qubit design shown in this paper should be readily adaptable to this and other types of existing multi-qubit architectures using either frequency-tuned gates or all-microwave gates. In order to avoid ohmic heating in larger architectures, the flux tuning must employ strictly superconducting wiring and may benefit from persistent-current operation at setpoints [48]. Notwithstanding such engineering issues, the qubit design presented here offers a scalable means to avoid both frequency crowding and flux-noise dephasing in multi-qubit gates, thus addressing a key challenge in realizing a logically-encoded qubit and fault-tolerant universal quantum computer.

## VI. ACKNOWLEDGMENTS

We acknowledge support from Intelligence Advanced Research Projects Activity (IARPA) under contract W911NF-16-0114. The device fabrication was performed in part at the Cornell NanoScale Facility, a member of the National Nanotechnology Coordinated Infrastructure (NNIC) which is supported by the National Science Foundation under Grant ECCS-1542081. We thank Y.-K.-K. Fung, J. Rohrs and J. R. Rozen for experimental contributions, and R. McDermott and T. Thorbeck for providing the SLUG amplifier and assistance with its setup. We also thank J.M. Gambetta, E. Magesan, R. McDermott, D.C. McKay and S. Rosenblatt for helpful discussions.

## Appendix A: Non-ideal fabrication in fixed frequency qubits

Lattices of coupled qubits are proposed to enable error-correction algorithms such as the ‘surface code’ [4, 5]. Qubits are arranged into a square grid with alternate qubits serving either data or error-checking functions. Bus-couplers provide interaction among adjacent qubits, with up to four qubits attached to each bus. A seven qubit-lattice thereby comprises 12 qubit pairs and a seventeen-qubit lattice comprises 34 pairs. However, single junction transmon qubits are challenging to fabricate with frequency precision of  $\sigma_f < 200$  MHz [25]. Such imprecision will inhibit functioning of qubit lattices. Considering a lattice of transmon qubits of frequency  $\sim 5$  GHz and anharmonicity  $\delta/2\pi = -340$  MHz, and considering cross-resonance gate operations, we can estimate the number of undesired interactions among these pairs. Studies of the cross-resonance gate [24] indicate that these gates will be dominated by undesirable interactions if the frequency separation  $|\Delta|$  between adjacent qubits is equal to zero, a degeneracy between  $f_{01}$  of the qubits; equal to  $-\delta/2\pi$ , a degeneracy between  $f_{01}$  of one qubit and  $f_{12}$  of the next; or if  $|\Delta| > -\delta/2\pi$  (weak interaction leading to very slow gate operation). In a simple Monte Carlo model, we assign to all points in the lattice a random qubit frequency from a gaussian distribution around 5 GHz, and count the number of degenerate or weak-interaction pairs, taking a range of  $\pm(\delta/2\pi)/20$ , or  $\pm 17$  MHz around each degeneracy. The results appearing in Table I make it evident that the likelihood of frequency collisions increases as the lattice grows.

| Number of QBs | $\sigma_f$                 | Mean Number of Collisions |
|---------------|----------------------------|---------------------------|
| 7             | $\frac{1}{2} \delta/2\pi $ | 2.3                       |
| 7             | $\frac{3}{4} \delta/2\pi $ | 3.6                       |
| 17            | $\frac{1}{2} \delta/2\pi $ | 6.6                       |
| 17            | $\frac{3}{4} \delta/2\pi $ | 10.6                      |

TABLE I. Frequency-collision modeling in lattices of transmon qubits employing cross-resonance gates. Predicted number of bad gate pairs (‘frequency collisions’) in two different lattice sizes. 7-qubit lattice has 12 pairs and 17-qubit lattice has 34 pairs. Mean of distribution is 5 GHz and two different distribution widths  $\sigma_f$  are considered.

## Appendix B: Qubit Coherence

For sample A, three  $T_1$  measurements were made at each flux point followed by three  $T_2^*$  measurements. At each flux point, the reported  $T_1$  and  $T_2^*$  values and error bars comprise the mean and standard deviation of the three measurements. The corresponding  $\Gamma_\phi$  value is found from these mean values and its error bar is found by propagating the errors in  $T_1$  and  $T_2^*$  through

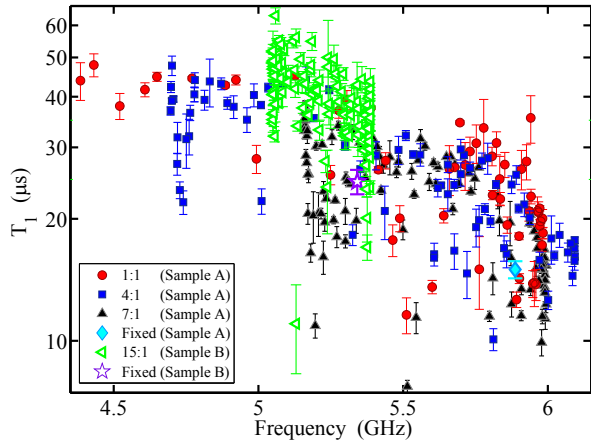


FIG. 5.  $T_1$  vs. frequency measured for all qubits discussed in the main paper. Single points included for  $T_1$  values measured for the fixed-frequency qubits.

via partial derivative and combining these in a quadrature sum. For sample B, at each flux point, first  $T_1$  was measured, then  $T_2^*$ , three times in succession. For this device the reported  $T_1$  and  $T_2^*$  values comprise the mean of the three measurements and the error bars are their standard deviation. Here the reported dephasing rate  $\Gamma_\phi$  comprises the mean  $\langle 1/T_2^* - 1/2T_1 \rangle$  found from the three  $T_1$ ,  $T_2^*$  pairs, and the error bar is the standard deviation. The uncertainties of the individual fits are significantly smaller than the standard deviation among several measurements, suggesting a time-variation in both  $T_1$  and  $T_2^*$ .

Figure 5 shows  $T_1$  plotted versus qubit frequency, measured for the qubits discussed in our paper. We observe a trend of increasing  $T_1$  with decreasing qubit frequency. In sample A, each qubit's quality factor  $\omega T_1$  is roughly constant, consistent with dielectric loss and a frequency-independent loss tangent, as observed in other tunable superconducting qubits [38]. On sample B,  $T_1$  decreases by about  $10 \mu\text{s}$  from the low to high end of the frequency range, consistent with Purcell loss to the readout resonator. In addition, fine structure is occasionally observed in Fig. 5 where  $T_1$  drops sharply at specific frequencies. These localized features in the  $T_1$  frequency dependence are observed for all tunable qubits that we have measured. These features, similar to those observed by [38], are attributed to frequencies where a qubit transition is resonant with a two-level system defect on or near the qubit. Additionally, on sample B, at a few frequency points inter-qubit coupling affects relaxation. When qubit  $Q_7$  is tuned to be nearly degenerate with fixed-frequency qubit  $Q_6$  (at  $\sim 5.33$  GHz) or to an adjacent tunable qubit  $Q_8$  (at  $\sim 5.22$  GHz), coupling via the adjacent buses produces an avoided crossing in the energy spectrum. This effect is barely noticeable in both the frequency curve of Fig. 2 as well as the relaxation

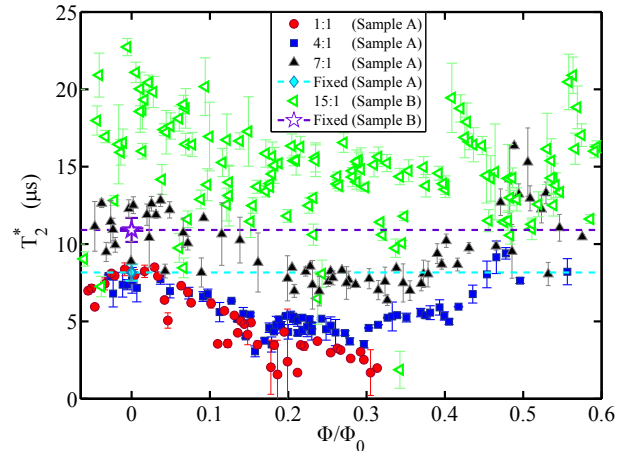


FIG. 6.  $T_2^*$  vs. flux measured for the qubits discussed in the main paper.  $T_2^*$  measured for the fixed-frequency qubits on both samples is included with dashed lines to help guide the eye.

data in Fig. 5.

Figure 6 shows  $T_2^*$  plotted versus flux, measured for the qubits discussed in our paper. For the tunable qubits on sample A,  $T_2^*$  is greatest at the qubit sweet-spots and decreases away from these sweet spots as  $D_\Phi$  increases. In the  $\alpha = 15$  tunable qubit ( $Q_7$ ) on sample B,  $T_2^*$  is nearly constant over the measured half flux quantum range. The small frequency dependence observed in  $T_2^*$  in sample B is consistent with the observed variation of  $T_1$  with frequency, leading to the frequency-independent dephasing rate observed for this qubit in Fig. 3.

### Appendix C: Relaxation Due to coupling to Flux Bias Line

Using a dc SQUID for the inductive element of a transmon allows for frequency-tuning via magnetic flux, but opens up a channel for energy relaxation into the dissipative environment across the bias coil, via the mutual inductance  $M$ . Koch et al. showed in Eq. (2.17) of Ref. [26] that the Josephson portion of the qubit Hamiltonian can be written in terms of a single phase variable with a shifted minimum that depends upon the qubit's asymmetry and the applied flux bias. By linearizing this Hamiltonian for small noise amplitudes about the static flux bias point, they compute the relaxation rate for a given current noise power related to the impedance  $R$  across the flux-bias coil and the mutual inductance between the coil and SQUID loop. Their analysis was presented for the case of a transmon containing a near-symmetrical SQUID. Here we apply their analysis to cases of increasing junction asymmetry, assuming harmonic oscillator wavefunctions for the qubit ground and excited state.

Using our typical device parameters ( $E_J/h = 20$  GHz,  $E_c/h = 350$  MHz,  $M = 2$  pH,  $R = 50 \Omega$ ) we obtain

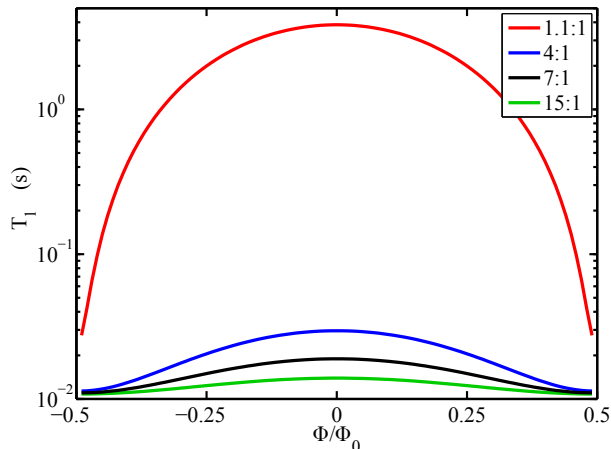


FIG. 7. Dependence of  $T_1$  with flux for asymmetric transmons, calculated for the asymmetries discussed in the main paper, due to coupling to an external flux bias following the analysis of Koch et al. [26]. Although in our experiments, the symmetric qubit had  $\alpha = 1$ , in this calculation  $\alpha = 1.1$  was used so that  $T_1$  did not diverge at  $\Phi = 0$ .

the resulting dependence of  $T_1$  as a function of bias flux, shown in Fig. 7 for the asymmetries discussed in our paper. For a 10% junction asymmetry, this contribution results in a  $T_1$  that varies between 25 ms and a few seconds, in agreement with Ref. [26]. As the junction asymmetry is increased, the minimum  $T_1$  value, obtained at odd half-integer multiples of  $\Phi_0$ , decreases, but even for our  $\alpha = 15$  qubit, the resulting  $T_1$  never falls below 10 ms, two orders of magnitude larger than the measured  $T_1$  due to all other mechanisms in current state-of-the-art superconducting qubits.

Also in Ref. [26], Koch et al. described a second loss channel for a transmon related to coupling to the flux-bias line. In this case, the relaxation occurs due to the oscillatory current through the inductive element of the qubit – independent of the presence of a SQUID loop – coupling to the flux-bias line, described by an effective mutual inductance  $M'$ . This mutual vanishes when the Josephson element of the qubit and the bias line are arranged symmetrically. With a moderate coupling asymmetry for an on-chip bias line, Koch et al. estimate that the  $T_1$  corresponding to this loss mechanism would be of the order of 70 ms. Because this mechanism does not directly involve the presence of a SQUID loop, this particular limit on  $T_1$  should be no different for an asymmetric-SQUID transmon as compared to a conventional transmon. An additional potential relaxation channel may arise due to capacitive coupling to the flux-bias line, as discussed in Ref. [39]. However, this is expected to be negligible where a remote wire-wound field coil is used, as in our experiments.

## Appendix D: Ramsey Decay Fitting

As described in Sec. IV, our analysis of qubit dephasing rates used a purely exponential fit to all of the measured Ramsey decays. Here we discuss why this fitting approach is appropriate for all asymmetric qubits and a large portion of the coherence data measured for the symmetric qubit.

Of all the qubits measured in this study, the symmetric  $\alpha = 1$  qubit was most affected by flux noise away from the qubit sweet spot because of its large energy-band gradient. Therefore, to illustrate the impact that flux noise has upon the Ramsey decay envelope we will consider the Ramsey measurements for this qubit on and off the sweet spot. Example measurements are shown at flux values of 0 and 0.3  $\Phi_0$  in Fig. 8a and b, respectively. At each flux point, we fit the Ramsey decay with both a purely exponential (Fig. 8a I) and purely Gaussian form (Fig. 8a II). The residuals of each fit are included to compare the quality of fit in each case. As has been discussed in the main paper, at the upper sweet-spot, where  $D_\Phi = 0$ , non-flux dependent background-dephasing should dominate and the Ramsey decay should be more readily fit using an exponential. Figure 8a shows that this is indeed the case: the purely exponential fit provides a more precise fit to the Ramsey decay, with the residuals to this fit being smaller over the entire range compared to those corresponding to the Gaussian fit. The Ramsey decay shown in Fig 8b was measured at a point where  $D_\Phi$  was the maximum measured for the  $\alpha = 1$  qubit. Here, it is clear that a purely Gaussian form results in a better fit with smaller residuals than an exponential envelope. This indicates that, at this flux point, the  $\alpha = 1$  qubit is heavily impacted by low-frequency flux noise, as a purely  $1/f$  dephasing source would result in a Gaussian envelope for the decay [9]. Although a purely Gaussian fit form is useful for illustrating the impact that flux noise has upon the Ramsey decay form, it is not an optimal quantitative approach for investigating dephasing in these qubits. This is because tunable transmons dephase not only due to flux noise with a roughly  $1/f$  power spectrum, but also due to other noise sources with different non- $1/f$  power spectra [35–37]. These other noise sources generally result in an exponential dephasing envelope. Also, dephasing has an intrinsic loss component that is always exponential in nature. Therefore, to accurately fit decay due to dephasing in these qubits, we must account for these exponential decay envelopes in any fitting approach that is not purely exponential.

To account for the  $T_1$  contribution to the Ramsey decay envelope in our non-exponential fitting, we take the average  $T_1$  measured at each flux point and separate this from  $T_2^*$  in the Ramsey fit function using  $1/T_2^* = 1/T_\phi + 1/2T_1$ . Therefore, instead of fitting a  $T_2^*$  time, we fit  $T_\phi$  directly. To fit the Ramsey decay using a Gaussian fit form, we square the dephasing exponent within the fitting function [Eq. (D1)]. We can go one step further by not forcing an explicit fit form to the dephas-

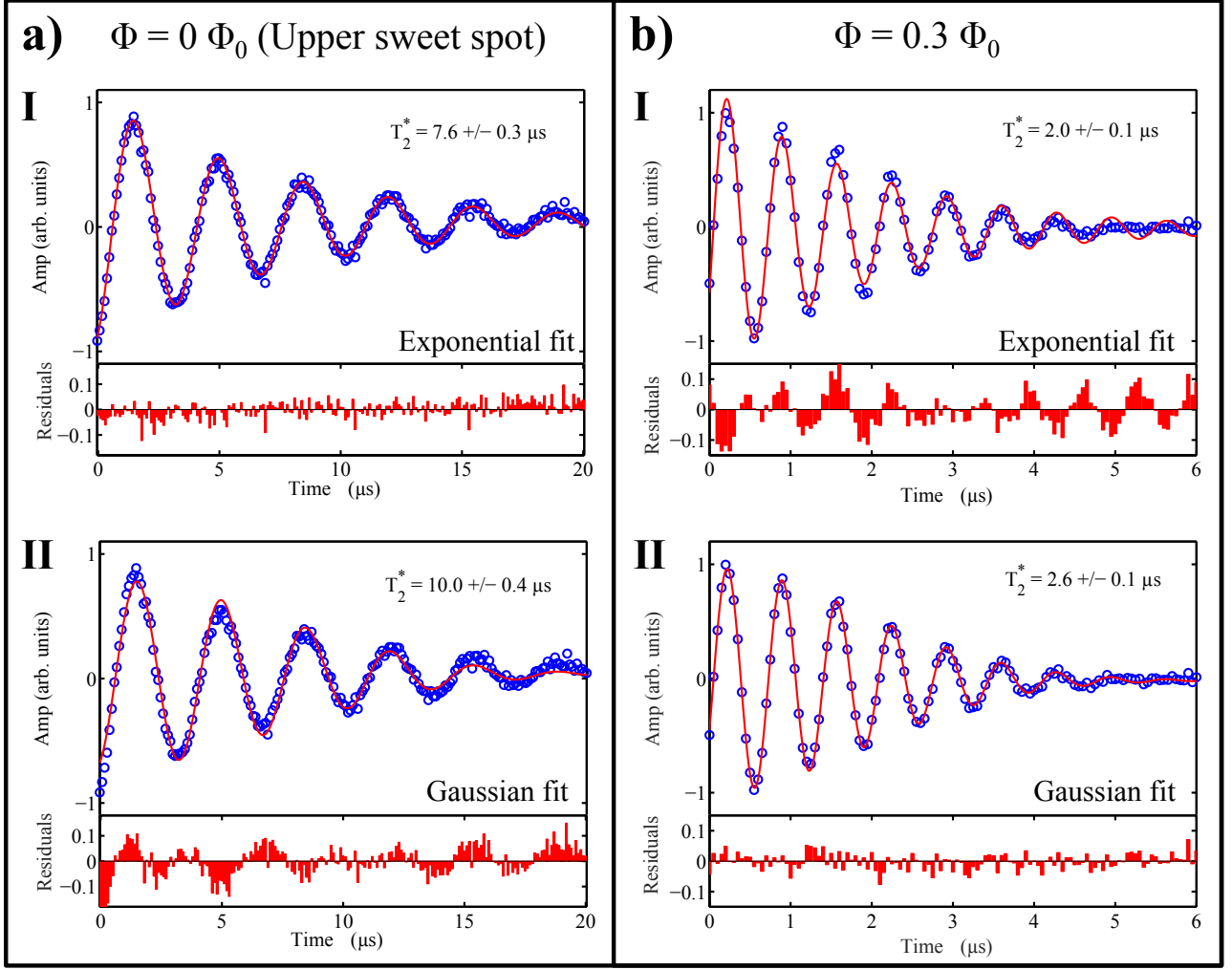


FIG. 8. Ramsey decay envelopes measured for the  $\alpha = 1$  qubit at a) the sweet-spot  $\Phi = 0$  and b)  $\Phi = 0.3\Phi_0$  where  $D_\Phi$  was the largest value measured for this qubit. At each flux point, the Ramsey decay envelopes are fit with both a purely exponential (I) and Gaussian (II) fit form. Functions fitted to the measured data (blue open circles) plotted as solid red lines.

ing exponent, but instead adding another fit parameter  $\gamma$  [Eq. (D2)], which would be 1 for a pure exponential and 2 for a pure Gaussian. Although a fit that is not explicitly exponential or Gaussian is not motivated directly by a particular theoretical model, by fitting Ramsey decays with this free exponent  $\gamma$ , we gain insight into the transition from flux-noise dominated dephasing at large  $D_\Phi$  to background dephasing near the sweet-spots. The two separate fit forms described above are given by the following decay functions:

$$f_{\text{Ramsey}}(t) = A + B\{\cos(\omega t + \delta) \exp(-\Gamma_1 t/2) \times \exp[-(\Gamma_\phi t)^\gamma]\}, \quad (\text{D1})$$

$$f_{\text{Ramsey}}(t) = A + B\{\cos(\omega t + \delta) \exp(-\Gamma_1 t/2) \times \exp[-(\Gamma_\phi t)^\gamma]\}, \quad (\text{D2})$$

where  $A$  and  $B$  are magnitude and offset constants to adjust the arbitrary measured signal,  $\omega$  is the detuning of the Ramsey pulses from the qubit frequency with a phase offset  $\delta$ ,  $\Gamma_1$  is the intrinsic loss rate ( $1/T_1$ ) and  $\Gamma_\phi$  is the dephasing rate. Here,  $A$ ,  $B$ ,  $\omega$ ,  $\delta$ ,  $\Gamma_\phi$ , and  $\gamma$  are fit parameters. All other components are fixed with values determined using the methods discussed above.

This behavior is illustrated in Fig. 9, where we plot  $\gamma$  vs. flux extracted from fits to the Ramsey measurements on the  $\alpha = 1$  qubit using Eq. (D1). In the flux region between  $\pm 0.1 \Phi_0$ ,  $\gamma \approx 1$ , indicating that the dephasing envelope is primarily exponential, and thus the dominant dephasing noise affecting the qubits here does not have a  $1/f$  spectrum. At flux bias points further away from the sweet-spot,  $\gamma$  shifts towards 2 as  $D_\Phi$  increases and appears to level off close to this value at flux biases above  $\sim 0.2 \Phi_0$ . Thus, in this bias regime, the dephasing envelope is primarily Gaussian and the dephasing noise influencing the qubits is predominantly low-frequency in

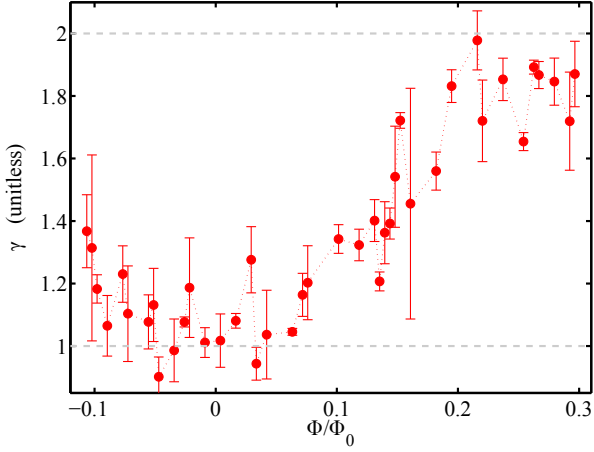


FIG. 9.  $\gamma$  vs flux extracted from fits to the Ramsey measurements on the  $\alpha = 1$  qubit using Eq. (D2).

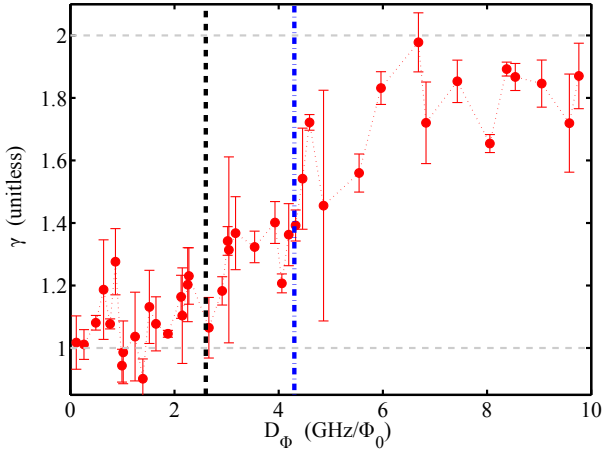


FIG. 10.  $\gamma$  vs  $D_\Phi$  extracted from fits to the Ramsey measurements on the  $\alpha = 1$  qubit using Eq. (D2). Dashed lines included to indicate the maximum  $D_\Phi$  reached by the  $\alpha = 7$  (black dashed line) and  $\alpha = 4$  (blue dot-dashed line) qubits measured on sample A.

nature with a  $1/f$ -like spectrum [7, 9].

We can also visualize this variable-exponent fit by plotting  $\gamma$  vs.  $D_\Phi$  rather than  $\Phi$ , again, for the  $\alpha = 1$  qubit (Fig. 10). In this plot,  $\gamma$  approaches 2 for  $D_\Phi$  values around 6  $\text{GHz}/\Phi_0$ . We have also included vertical dashed lines on Fig. 10 indicating the maximum  $D_\Phi$  values reached by the less tunable  $\alpha = 4$  and 7 qubits on sample A. Below these  $D_\Phi$  levels,  $\gamma$  is close to 1 implying that the decay envelope is nearly exponential, and thus justifying our use of an exponential decay for fitting the asymmetrical qubits in the main paper.

As yet another approach to fitting the Ramsey decay envelopes, we can employ a function that separates the exponential dependence from background-dephasing

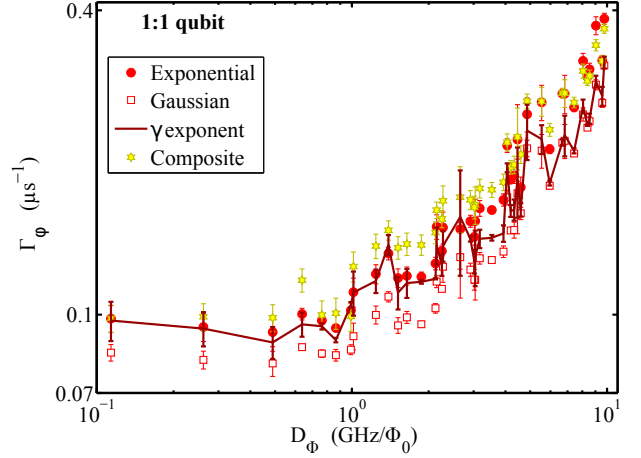


FIG. 11.  $\Gamma_\phi$  vs.  $D_\Phi$  calculated for the  $\alpha = 1$  qubit using the exponential, Gaussian [Eq. (D1)],  $\gamma$ -exponent [Eq. (D2)], and composite [Eq. (D3)] fitting forms.

from the Gaussian form due to dephasing from noise with a low-frequency tail. For this fit, along with separating out the  $T_1$  contribution to the Ramsey decay envelope, we also determine the non-flux dependent background-dephasing rate at the sweet-spot, then use this rate as a fixed parameter in the fitting of our Ramsey measurements at any given flux point. We now have a composite Ramsey fit form that has three components: a  $T_1$  contribution and background dephasing component that are purely exponential and fixed by the fitting of separate measurements, plus a Gaussian component to capture the dephasing due to noise with a  $1/f$  spectrum. This leads to a composite fitting function of the form:

$$f_{\text{Ramsey}}(t) = A + B\{\cos(\omega t + \delta) \exp(-\Gamma_1 t/2) \times \exp(-\Gamma_{\phi, \text{bkg}} t) \exp[-(\Gamma_\phi t)^2]\}, \quad (\text{D3})$$

where  $A$  and  $B$  are magnitude and offset constants to adjust the arbitrary measured signal,  $\omega$  is the detuning from the qubit frequency with a phase offset  $\delta$ ,  $\Gamma_1$  is the intrinsic loss rate ( $1/T_1$ ),  $\Gamma_{\phi, \text{bkg}}$  is the background dephasing rate measured at  $D_\Phi = 0$  and  $\Gamma_\phi$  is the fitted dephasing rate. Here,  $A$ ,  $B$ ,  $\omega$ ,  $\delta$ , and  $\Gamma_\phi$  are fit parameters. All other components are fixed with values determined using methods discussed above. Though this fit form well separates the different components to dephasing decay, it has one key deficiency: it assumes that the background dephasing rate is frequency independent, which is not necessarily justified, as the background dephasing mechanism may also vary with frequency. To calculate the total dephasing rate using this fit form, we add the constant background dephasing to the fitted  $\Gamma_\phi$ .

To understand how the explicit fitting form impacts the dephasing rate, in Fig. 11 we plot  $\Gamma_\phi$  vs.  $D_\Phi$  calculated for the  $\alpha = 1$  qubit using the four different fitting forms: exponential, Gaussian [Eq. (D1)],  $\gamma$ -exponent

[Eq. (D2)], and composite [Eq. (D3)]. We first note that any differences in the rate of dephasing calculated at each point using the various fit methods are subtle and the fits are reasonably consistent with one another within the fit error bars and scatter. We do observe, though, that a purely exponential fit results in a dephasing rate that is slightly higher than the values from the Gaussian fits for all flux points, resulting in the largest slope and thus the highest effective flux-noise level. Therefore, we conclude that forcing a purely exponential fit to the Ramsey decay envelopes measured for qubits that are strongly influenced by  $1/f$  flux noise simply puts an upper bound on the absolute flux noise strength. The  $\gamma$ -exponent fitting approach provides a dephasing rate that agrees well with that extracted from the exponential fit form at low  $D_\Phi$  values where background-dephasing processes dominate. However, at higher  $D_\Phi$  values where the qubit is heavily impacted by  $1/f$  flux noise, the  $\gamma$ -exponent fit provides better agreement with the Gaussian-fitted dephasing rate.

The composite fit is rigidly fixed in the  $\Gamma_\phi$  axis by the value chosen to match the background dephasing rate, in this case chosen to match the rate observed at the lowest  $D_\Phi$  for the pure exponential fit. For this reason, direct comparisons at individual flux points between this fit and the others are more difficult. Despite all of these potential issues, the slope of  $\Gamma_\phi$  vs.  $D_\Phi$  is independent of the chosen background-dephasing rate. Therefore, this composite fit can be used to calculate a flux-noise level for this  $\alpha = 1$  qubit that takes into account both the exponential nature of non-flux dependent dephasing and the Gaussian nature of  $1/f$  flux-noise decay. Using the same methods outlined above, where we specified  $\Gamma_\phi = 2\pi\sqrt{A_\Phi}|\ln(2\pi f_{IRt})|D_\Phi$ , following the approach described in Ref. [9], we use the slope of this composite fit to extract a  $1/f$  flux noise level of  $A_\Phi^{1/2} = 1.3 \pm 0.2 \mu\Phi_0$ .

This  $\sim 10\%$  reduction in the extracted flux-noise level for the  $\alpha = 1$  qubit compared to the purely exponential fit ( $A_\Phi^{1/2} = 1.4 \pm 0.2 \mu\Phi_0$ ) brings it closer to the flux-noise level extracted from the fits to the measurements on the  $\alpha = 7$  and 4 qubits:  $1.3 \pm 0.2 \mu\Phi_0$  and  $1.2 \pm 0.2 \mu\Phi_0$ , respectively. The Ramsey measurements for these qubits were fit using a purely exponential fit form. It is important to note though, that the  $\sim 10\%$  reduction in the composite fit extracted flux-noise level for the  $\alpha = 1$  qubit is within the errors associated with our flux-noise calculations.

To conclude this fitting study, we have shown that:

1. The  $\alpha = 1$  qubit in this study has a Ramsey decay envelope that is more Gaussian in nature at high  $D_\Phi$  values where the dephasing of this qubit is strongly influenced by low-frequency flux noise.
2. Although we have discussed different fitting approaches that better model the Ramsey decay envelope of qubits influenced by  $1/f$  flux-noise, using a purely exponential decay form for the Ramsey decay simply puts an upper bound on the extracted flux noise strength. Also, the value of the flux-noise level and the dephasing rates are comparable to those we obtained with the various other fitting approaches.
3. Using a Ramsey fit function that takes into account both the exponential nature of the  $T_1$  contribution to the decay envelope and non-flux dependent dephasing, as well as the Gaussian nature of dephasing due to  $1/f$  flux noise, allows us to calculate a flux noise level for the  $\alpha = 1$  qubit that agrees well with the other, asymmetric qubits on the same sample. This is expected, as qubits of the same geometry on the same chip should experience similar flux noise [14].

- 
- [1] R. Barends, J. Kelly, A. Megrant, A. Veitia, D. Sank, E. Jeffrey, T. C. White, J. Mutus, A. G. Fowler, B. Campbell, Y. Chen, B. Chiaro, A. Dunsworth, C. Neill, P. O'Malley, P. Roushan, A. Vainsencher, J. Wenner, A. N. Korotkov, A. N. Cleland, and M. J. Martinis, Superconducting quantum circuits at the surface code threshold for fault tolerance, *Nature (London)* **508**, 500 (2014).
- [2] J. Kelly, R. Barends, A. G. Fowler, A. Megrant, E. Jeffrey, T. C. White, D. Sank, J. Y. Mutus, B. Campbell, Y. Chen, Z. Chen, B. Chiaro, A. Dunsworth, I. C. Hoi, C. Neill, P. O'Malley, C. Quintana, P. Roushan, A. Vainsencher, J. Wenner, A. N. Cleland, and J. M. Martinis, State preservation by repetitive error detection in a superconducting quantum circuit, *Nature (London)* **519**, 66 (2015).
- [3] A. D. Córcoles, E. Magesan, S. J. Srinivasan, A. W. Cross, M. Steffen, J. M. Gambetta, and J. M. Chow, Demonstration of a quantum error detection code using a square lattice of four superconducting qubits, *Nat. Commun.* **6** (2015).
- [4] J. M. Gambetta, J. M. Chow, and M. Steffen, Building logical qubits in a superconducting quantum computing system, *npj Quant. Inf.* **3**, 2 (2017).
- [5] A. G. Fowler, M. Mariantoni, J. M. Martinis, and A. N. Cleland, Surface codes: Towards practical large-scale quantum computation, *Phys. Rev. A* **86**, 032324 (2012).
- [6] S. M. Anton, C. Müller, J. S. Birenbaum, S. R. Okelley, A. D. Fefferman, D. S. Golubev, G. C. Hilton, H. M. Cho, K. D. Irwin, F. C. Wellstood, G. Schön, A. Shnirman, and J. Clarke, Pure dephasing in flux qubits due to flux noise with spectral density scaling as  $1/f_\alpha$ , *Phys. Rev. B* **85**, 224505 (2012).
- [7] F. Yoshihara, K. Harrabi, A. O. Niskanen, Y. Nakamura, and J. S. Tsai, Decoherence of flux qubits due to  $1/f$  flux noise, *Phys. Rev. Lett.* **97**, 167001 (2006).

- [8] J. Bylander, S. Gustavsson, F. Yan, F. Yoshihara, K. Harrabi, G. Fitch, D. G. Cory, Y. Nakamura, J. S. Tsai, and W. D. Oliver, Noise spectroscopy through dynamical decoupling with a superconducting flux qubit, *Nat. Phys.* **7**, 565 (2011).
- [9] G. Ithier, E. Collin, P. Joyez, P. J. Meeson, D. Vion, D. Esteve, F. Chiarello, A. Shnirman, Y. Makhlin, J. Schrieffer, and G. Schon, Decoherence in a superconducting quantum bit circuit, *Phys. Rev. B* **72**, 134519 (2005).
- [10] E. Paladino, Y. M. Galperin, G. Falci, and B. L. Altshuler,  $1/f$  noise: Implications for solid-state quantum information, *Rev. Mod. Phys.* **86**, 361 (2014).
- [11] J. M. Martinis, S. Nam, J. Aumentado, K. M. Lang, and C. Urbina, Decoherence of a superconducting qubit due to bias noise, *Phys. Rev. B* **67**, 094510 (2003).
- [12] F. C. Wellstood, C. Urbina, and J. Clarke, Low-frequency noise in dc superconducting quantum interference devices below 1 K, *Appl. Phys. Lett.* **50**, 772 (1987).
- [13] C. M. Quintana, Y. Chen, D. Sank, A. G. Petukhov, T. C. White, D. Kafri, B. Chiaro, A. Megrant, R. Barends, B. Campbell, Z. Chen, A. Dunsworth, A. G. Fowler, R. Graff, E. Jeffrey, J. Kelly, E. Lucero, J. Y. Mutus, M. Neeley, C. Neill, P. J. J. O'Malley, P. Roushan, A. Shabani, V. N. Smelyanskiy, A. Vainsencher, J. Wenner, H. Neven, and J. M. Martinis, Observation of classical-quantum crossover of  $1/f$  flux noise and its paramagnetic temperature dependence, *Phys. Rev. Lett.* **118**, 057702 (2017).
- [14] S. Sendelbach, D. Hover, A. Kittel, M. Mück, J. M. Martinis, and R. McDermott, Magnetism in squids at millikelvin temperatures, *Phys. Rev. Lett.* **100**, 227006 (2008).
- [15] L. Faoro and L. B. Ioffe, Microscopic origin of low-frequency flux noise in josephson circuits, *Phys. Rev. Lett.* **100**, 227005 (2008).
- [16] H. Wang, C. Shi, J. Hu, S. Han, C. C. Yu, and R. Q. Wu, Candidate source of flux noise in squids: adsorbed oxygen molecules, *Phys. Rev. Lett.* **115**, 077002 (2015).
- [17] S. LaForest and R. de Sousa, Flux-vector model of spin noise in superconducting circuits: Electron versus nuclear spins and role of phase transition, *Phys. Rev. B* **92**, 054502 (2015).
- [18] L. DiCarlo, J. M. Chow, J. M. Gambetta, L. S. Bishop, B. R. Johnson, D. I. Schuster, J. Majer, A. Blais, L. Frunzio, S. M. Girvin, and S. R. J., Demonstration of two-qubit algorithms with a superconducting quantum processor, *Nature (London)* **460**, 240 (2009).
- [19] J. M. Martinis and M. R. Geller, Fast adiabatic qubit gates using only  $\sigma_z$  control, *Phys. Rev. A* **90**, 022307 (2014).
- [20] C. Rigetti and M. Devoret, Fully microwave-tunable universal gates in superconducting qubits with linear couplings and fixed transition frequencies, *Phys. Rev. B* **81**, 134507 (2010).
- [21] J. M. Chow, A. D. Córcoles, J. M. Gambetta, C. Rigetti, B. R. Johnson, J. A. Smolin, J. R. Rozen, G. A. Keefe, M. B. Rothwell, M. B. Ketchen, and M. Steffen, Simple all-microwave entangling gate for fixed-frequency superconducting qubits, *Phys. Rev. Lett.* **107**, 080502 (2011).
- [22] J. M. Chow, J. M. Gambetta, E. Magesan, D. W. Abraham, A. W. Cross, B. R. Johnson, N. A. Masluk, C. A. Ryan, J. A. Smolin, S. J. Srinivasan, and M. Steffen, Implementing a strand of a scalable fault-tolerant quantum computing fabric, *Nat. Commun.* **5** (2014).
- [23] S. Sheldon, E. Magesan, J. M. Chow, and J. M. Gambetta, Procedure for systematically tuning up cross-talk in the cross-resonance gate, *Phys. Rev. A* **93**, 060302 (2016).
- [24] J. M. Gambetta, *Control of Superconducting Qubits*, chap. B4, Lecture Notes of the 44th IFF Spring School (2013).
- [25] S. Rosenblatt, J. Hertzberg, M. Brink, J. Chow, J. Gambetta, Z. Leng, A. Houck, J. Nelson, B. Plourde, X. Wu, R. Lake, J. Shainline, D. Pappas, U. Patel, and R. McDermott, Y46.00002 : Variability metrics in josephson junction fabrication for quantum computing circuits, APS March Meeting, New Orleans, LA (2017).
- [26] J. Koch, T. M. Yu, J. Gambetta, A. A. Houck, D. I. Schuster, J. Majer, A. Blais, M. H. Devoret, S. M. Girvin, and R. J. Schoelkopf, Charge-insensitive qubit design derived from the cooper pair box, *Phys. Rev. A* **76**, 042319 (2007).
- [27] J. D. Strand, M. Ware, F. Beaudoin, T. A. Ohki, B. R. Johnson, A. Blais, and B. L. T. Plourde, First-order sideband transitions with flux-driven asymmetric transmon qubits, *Phys. Rev. B* **87**, 220505 (2013).
- [28] M. Takita, A. D. Córcoles, E. Magesan, B. Abdo, M. Brink, A. Cross, J. M. Chow, and J. M. Gambetta, Demonstration of weight-four parity measurements in the surface code architecture, *Phys. Rev. Lett.* **117**, 210505 (2016).
- [29] IBM Quantum Experience, <http://www.research.ibm.com/quantum/> (2017).
- [30] S. M. Anton, J. S. Birenbaum, S. R. O'Kelley, V. Bolkhovskoy, D. A. Braje, G. Fitch, M. Neeley, G. C. Hilton, H.-M. Cho, K. D. Irwin, F. C. Wellstood, W. D. Oliver, A. Shnirman, and J. Clarke, Magnetic flux noise in dc squids: Temperature and geometry dependence, *Phys. Rev. Lett.* **110**, 147002 (2013).
- [31] R. McDermott, private communication.
- [32] S. Sheldon, L. S. Bishop, E. Magesan, S. Filipp, J. M. Chow, and J. M. Gambetta, Characterizing errors on qubit operations via iterative randomized benchmarking, *Phys. Rev. A* **93**, 012301 (2016).
- [33] D. Hover, S. Zhu, T. Thorbeck, G. J. Ribeill, D. Sank, J. Kelly, R. Barends, J. M. Martinis, and R. McDermott, High fidelity qubit readout with the superconducting low-inductance undulatory galvanometer microwave amplifier, *Appl. Phys. Lett.* **104**, 152601 (2014).
- [34] M. D. Reed, L. DiCarlo, B. R. Johnson, L. Sun, D. I. Schuster, L. Frunzio, and R. J. Schoelkopf, High-fidelity readout in circuit quantum electrodynamics using the jaynes-cummings nonlinearity, *Phys. Rev. Lett.* **105**, 173601 (2010).
- [35] A. P. Sears, A. Petrenko, G. Catelani, L. Sun, H. Paik, G. Kirchmair, L. Frunzio, L. I. Glazman, S. M. Girvin, and R. J. Schoelkopf, Photon shot noise dephasing in the strong-dispersive limit of circuit qed, *Phys. Rev. B* **86**, 180504 (2012).
- [36] D. I. Schuster, A. Wallraff, A. Blais, L. Frunzio, R. S. Huang, J. Majer, S. M. Girvin, and R. J. Schoelkopf, ac stark shift and dephasing of a superconducting qubit strongly coupled to a cavity field, *Phys. Rev. Lett.* **94**, 123602 (2005).
- [37] J. Gambetta, A. Blais, D. I. Schuster, A. Wallraff, L. Frunzio, J. Majer, M. H. Devoret, S. M. Girvin, and R. J. Schoelkopf, Qubit-photon interactions in a cavity

- measurement-induced dephasing and number splitting, *Phys. Rev. A* **74**, 042318 (2006).
- [38] R. Barends, J. Kelly, A. Megrant, D. Sank, E. Jeffrey, Y. Chen, Y. Yin, B. Chiaro, J. Mutus, C. Neill, P. O'Malley, P. Roushan, J. Wenner, T. C. White, A. N. Cleland, and J. M. Martinis, Coherent josephson qubit suitable for scalable quantum integrated circuits, *Phys. Rev. Lett.* **111**, 080502 (2013).
- [39] B. R. Johnson, *Controlling Photons in Superconducting Electrical Circuits*, Ph.D. thesis, Yale University (2011).
- [40] Y. Makhlin, G. Schön, and A. Shnirman, Quantum-state engineering with josephson-junction devices, *Rev. Mod. Phys.* **73**, 357 (2001).
- [41] Y. Makhlin and A. Shnirman, Dephasing of solid-state qubits at optimal points, *Phys. Rev. Lett.* **92**, 178301 (2004).
- [42] D. J. Van Harlingen, T. L. Robertson, B. L. T. Plourde, P. A. Reichardt, T. A. Crane, and J. Clarke, Decoherence in josephson-junction qubits due to critical-current fluctuations, *Phys. Rev. B* **70**, 064517 (2004).
- [43] J.-L. Orgiazzi, C. Deng, D. Layden, R. Marchildon, F. Kitapli, F. Shen, M. Bal, F. R. Ong, and A. Lupascu, Flux qubits in a planar circuit quantum electrodynamics architecture: Quantum control and decoherence, *Phys. Rev. B* **93**, 104518 (2016).
- [44] M. Stern, G. Catelani, Y. Kubo, C. Grezes, A. Bienfait, D. Vion, D. Esteve, and P. Bertet, Flux qubits with long coherence times for hybrid quantum circuits, *Phys. Rev. Lett.* **113**, 123601 (2014).
- [45] R. C. Bialczak, R. McDermott, M. Ansmann, M. Hofheinz, N. Katz, E. Lucero, M. Neeley, A. D. O'Connell, H. Wang, A. N. Cleland, and J. M. Martinis,  $1/f$  flux noise in josephson phase qubits, *Phys. Rev. Lett.* **99**, 187006 (2007).
- [46] S. Sendelbach, D. Hover, M. Mück, and R. McDermott, Complex inductance, excess noise, and surface magnetism in dc squids, *Phys. Rev. Lett.* **103**, 117001 (2009).
- [47] P. Kumar, S. Sendelbach, M. A. Beck, J. W. Freeland, Z. Wang, H. Wang, C. C. Yu, R. Q. Wu, D. P. Pappas, and R. McDermott, Origin and reduction of  $1/f$  magnetic flux noise in superconducting devices, *Phys. Rev. Appl.* **6**, 041001 (2016).
- [48] G. Keefe, R. Koch, F. Milliken, and J. Rozen, Persistent current switch. US Patent 8138880 (2012).